stantial distortion in the bath surface. As can be seen in the front and side views (Fig. 3), the initial contact again takes the form of a localized filament. As the cylinder approaches the bath, the filament thickens and the coalesced region moves outward from the point of first contact, zippering the two bodies of fluid together. This qualitative picture is also seen in a variety of other cylinder coalescence events we have simulated, including a weak four-roller flow, where the merger is driven for the most part by surface tension.

The Eulerian velocity field can be obtained by accumulating the average molecular velocities in a fixed array of sampling bins, averaged over the direction of the cylinder axis. The result (Fig. 4) shows the expected dipole vortex flow as the cylinder displaces bath fluid. At earlier and later times the velocity field indicates the drop descending and the bath fluid splashing upward, respectively. The dynamics of the splash, although interesting in itself (*10*), is awkward to study because a large bath is required and this is too costly in number of molecules and computer resources. The stress tensor has also been calculated in this flow but is too sensitive to thermal fluctuations to provide a clear signal.

The present set of simulations is, in a sense, on the edge of the continuum because average quantities such as shapes can be studied in detail, but the Navier-Stokes fields are often too noisy to resolve. Expected advances in computing power in the near future should overcome these difficulties, and we can look forward to systematic calculations of fluid phenomena on all interesting length scales.

REFERENCES AND NOTES

1. G. E. Charles and S. G. Mason, *J. Colloid Sci.* **14**, 105 (1960).
2. J. C. Lee and T. D. Hodgson, *Chem. Eng. Sci.* **23**, 1375 (1968).
3. G. V. Jeffreys and G. A. Davies, in *Recent Advances in Liquid-Liquid Extraction*, C. Hanson, Ed. (Pergamon, New York, 1971), pp. 495–584.
4. H. N. Oguz and A. Prosperetti, *J. Fluid Mech.* **203**, 149 (1989).
5. T. S. Sorensen, Ed., *Dynamics and Instability of Fluid Interfaces* (Springer-Verlag, New York, 1979).
6. M. P. Allen and D. J. Tildesley, *Computer Simulation of Liquids* (Oxford Univ. Press, Oxford, 1987).
7. J. Koplik, J. R. Banavar, J. F. Willemsen, *Phys. Fluids A* **1**, 781 (1989).
8. P. A. Thompson and M. O. Robbins, *Phys. Rev. Lett.* **63**, 766 (1989).
9. G. I. Taylor, *Proc. R. Soc. London Ser. A* **146**, 501 (1934).
10. A. M. Worthington, *A Study of Splashes* (Macmillan, New York, 1963).

11. This research was supported by the National Aeronautics and Space Administration Microgravity Program and the National Science Foundation Fluid, Particulate, and Hydraulic Systems Program, and the facilities of the Pittsburgh Supercomputer Center.

8 May 1992; accepted 7 July 1992

Rapid Intraplate Strain Accumulation in the New Madrid Seismic Zone

Lanbo Liu, Mark D. Zoback, Paul Segall*

Remeasurement of a triangulation network in the southern part of the New Madrid seismic zone with the Global Positioning System has revealed rapid crustal strain accumulation since the 1950s. This area experienced three large (moment magnitudes >8) earthquakes in 1811 to 1812. The orientation and sense of shear is consistent with right-lateral strike slip motion along a northeast-trending fault zone (as indicated by current seismicity). Detection of crustal strain accumulation may be a useful discriminant for identifying areas where potentially damaging intraplate earthquakes may occur despite the absence of large earthquakes during historic time.

The rate at which elastic strain energy accumulates controls how often large earthquakes can occur. Although strain rates in intraplate regions must, in general, be quite low (*1*), in areas such as the New Madrid, Missouri, and Charleston, South Carolina, seismic zones, strain rates must be relatively rapid if paleoseismic evidence indicating the occurrence of damaging earthquakes every 500 to 1000 years (*2*, *3*) represents repeated slip on the same faults (*4*). In this study, we report measurements of the crustal strain accumulation rate in a portion of the New Madrid seismic zone (NMSZ). Historically, the NMSZ is the most active seismic zone in the midcontinent region east of the Rocky Mountains in the United States (*5*). Three large earthquakes occurred in December 1811 and January and February 1812. The estimated moment magnitudes (M) were all between M = 8.1 and M = 8.3 (*6*). We studied an area located along an approximately 100-km zone of seismicity (*7*) that trends to the northeast between Marked Tree, Arkansas, and Caruthersville, Missouri (Fig. 1). This zone coincides with a reactivated fault zone detected by seismic reflection profiling (*8*); the fault zone is centered along a major crustal rift originally formed in late Precambrian to early Paleozoic time (*9*). The inferred patterns of ground shaking and damage suggest that at least one (and possibly two) of the three major 1811 and 1812 earthquakes (indicated by the large gray dots in Fig. 1) were located along this segment of the NMSZ (*10*). Focal plane mechanisms of recent minor earthquakes indicate that overall motion is right-lateral strike slip along this fault trend (*11*). The result is consistent with the east-northeast to west-southwest direction of maximum horizontal stress in this region (*12*).

First- and second-order triangulation networks were established in this area as early as 1929 for engineering and mapping purposes. In the early 1950s, a much wider area was surveyed with the use of first- and second-order triangulation (*13*). Although crustal deformation can be measured with repeated angle measurements from the triangulation data alone (*14*) [as in (*4*)], there were insufficient repeated angles in this region to compute strain. We conducted a new survey of many of the triangulation stations with the Global Positioning System (GPS) in 1991. This made it possible to determine whether detectable crustal strain had accumulated during the past 35 to 40 years. With the use of dual-frequency GPS receivers, relative distances between bench marks can generally be determined to within several millimeters over the approximately 10-km baselines of the original triangulation network (*15*). In contrast, the precision of first-order triangulation is equivalent to several centimeters over approximately 10-km baselines.

We visited about 100 stations to recover the bench marks from the old surveys and found that many of the bench marks had been destroyed by either road construction or cultivation. An interconnected network of about 20 stations was found in good condition to the west of the town of Caruthersville (hereafter termed the Caruthersville network) that straddled both the northeast-trending zone of seismicity and the northwest boundary of the rift (Fig. 1). Although some scattered seismicity falls along the rift boundaries, the rift boundaries are not well defined by instrumentally recorded seismicity (Fig. 1). Most of the bench marks in the Caruthersville network had been surveyed in either January 1953 or May 1955. A new GPS survey of this area was made in March and April 1991. Each station was occupied twice (2 to 3 weeks apart) for an approximately 6-hour recording session. In the case of four bench marks (solid triangles in Fig. 1), satellite visibility was restricted by trees and buildings; consequently, remote stations were used or

Department of Geophysics, Stanford University, Stanford, CA 94305.

*Also at U.S. Geological Survey, Menlo Park, CA 94025.

Table 1. Strain rates (ppm per year) computed of the Caruthersville network (*34*).

Data	$\dot{\gamma}_1$	$\dot{\gamma}_2$	$\dot{\gamma}$	95% confidence interval	ϕ	σ_0
All data	−0.076 ± 0.027	−0.077 ± 0.027	0.108	0.042 to 0.197	67.2° ± 7.7°	1.52
W. subnet	−0.247 ± 0.047	−0.018 ± 0.040	0.248	0.118 to 0.395	87.8° ± 4.7°	1.56
E. subnet	−0.013 ± 0.037	−0.111 ± 0.037	0.111	0.036 to 0.215	48.3° ± 9.4°	1.34

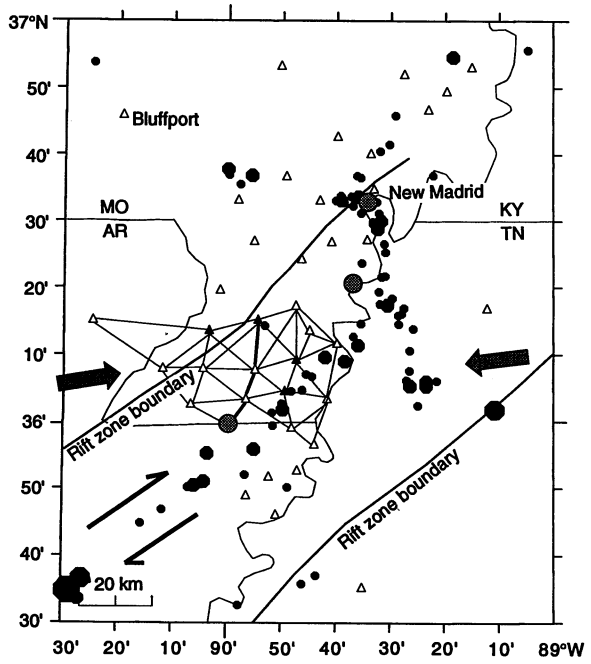

Fig. 1. Generalized map of the NMSZ. Well-located earthquake epicenters are shown as a function of size, as are the approximate locations of large (M ~8.1 to 8.3) earthquakes of 1811 to 1812 (*10*) (locations indicated by the large gray dots). The boundaries of the reactivated crustal rift zone within which the New Madrid seismicity occurs, termed the Reelfoot rift, are shown as determined from aeromagnetic data (*9*). The open triangles indicate triangulation bench marks reoccupied in the 1991 GPS field survey. Those connected by lines indicate the network, chosen for this study, that overlies both the right-lateral strike slip fault zone (*11*) running down the center of the rift and the northwest rift boundary. Right-lateral strike slip faulting on northeast-trending vertical faults is consistent with east to northeast regional compression (large arrows) (*12*). The four solid triangles denote the stations reoccupied by GPS receivers at remote marks, and the thick line divides the eastern and the western subnetworks.

established (typically a few tens of meters away) that were tied back to the main bench marks with the use of conventional surveying techniques.

Using Bernese software (*16*) with broadcast satellite orbits (*17*), we reduced the GPS data. Baseline vectors were obtained for each station relative to a reference station established at Bluffport, approximately 70 km to the northwest (Fig. 1). We used the simultaneous reduction method (*18, 19*) to calculate the horizontal shear strain rate $\dot{\gamma}$, the time-derivative of the maximum horizontal shear strain γ. The maximum horizontal shear strain γ and the orientation of the principal compression ϕ were defined as

$$\gamma = (\gamma_1^2 + \gamma_2^2)^{1/2}$$
$$\text{and } \phi = 0.5 \tan^{-1}(-\gamma_2/\gamma_1) \quad (1)$$

where γ_1 and γ_2 are the engineering shear strain components defined by

$$\gamma_1 = \epsilon_{EE} - \epsilon_{NN} \text{ and } \gamma_2 = \epsilon_{EN} + \epsilon_{NE} \quad (2)$$

where ϵ_{EE}, ϵ_{NN}, ϵ_{EN}, and ϵ_{NE} are the tensor strain components in the horizontal plane. The subindices E and N denote east and north, respectively. In general, the simultaneous reduction method can be used to calculate all four components of strain and two components of the tilt (*19*). However, the original triangulation survey data do not provide control on dilatation, rotation, or tilt. Use of Frank's method for computing strain (*14, 20*) gave results similar to those from the simultaneous reduction method.

We used all of the triangulation data from the 1950s, with the exception of five blunders clearly labeled in the National Geodetic Survey (NGS) database. These data yielded 181 horizontal direction observations for the 17 stations in the Caruthersville network. The GPS observations yield 17 independent baseline vectors between pairs of the 18 stations (the Caruthersville network plus Bluffport, the base station) during each occupation, for a total of 34 baseline vectors. The strain is estimated with the use of the horizontal directions and the two sets of GPS baseline vectors. The covariance matrices of the GPS baseline vectors are scaled to be consistent with the reputability in the two surveys (*21*). As indicated in Table 1 and Fig. 2, significant strain has accumulated across the Caruthersville network since the 1950s. We can reject the hypothesis that no strain occurred ($\dot{\gamma}_1 = 0$; $\dot{\gamma}_2 = 0$) at the 95% confidence level (Fig. 2). The measured shear strain rates are quite large, roughly one-third of the average strain rate in the San Andreas fault system (*22*) and about two orders of magnitude higher than estimated plate-wide average strain rates. In an attempt to discriminate strain accumulation associated with the seismicity trend and the northwest boundary of the rift, we broke the Caruthersville network in half by defining eastern and western subnetworks (divided by the heavy line in Fig. 1). Surprisingly, strain rates were higher in the western subnetwork straddling the northwest boundary of the rift than in the eastern subnetwork straddling the seismicity trend. However, the difference in strain rates in the two areas is not significant (Fig. 2). The strain rate in the western subnet is significant at the 95% confidence level, whereas in the eastern subnet it is not.

We believe that three lines of evidence provide additional support for our findings of unusually high strain rates in this area. First, the strain rates computed for both the eastern and western subnetworks are comparable in magnitude and direction, although they do not share any common data. Second, the observed orientation and sense of shear is consistent with the regional east-northeast to east-west maximum horizontal compressive stress direction in this area (*12*) and the known sense of shear associated with earthquakes along the Caruthersville to Marked Tree seismicity trend (*11*). Third, inversion of the observed angle changes to derive station displacements (*23*) shows that the displacements are consistent with right-lateral strike slip motion at depth on planes striking subparallel to the trend of the Caruthersville to Marked Tree seismicity. The displacement vectors showed that the computed strain results from broadly distributed displacements and is not caused by just a few large, and possibly erroneous, station displacements.

In contrast to these findings, Snay, Ni, and Neugebauer (*24*), using the same types of data and analysis techniques, found that the rate of strain accumulation across the northern NMSZ is about one-half of that from the Caruthersville network. Their estimated strain rate does not differ statistically from zero at the 95% confidence level. It appears, therefore, that there are spatial variations in the rate of strain accumulation in the NMSZ.

As is the case along transform plate boundaries like the San Andreas, it is likely that the high rate of accumulation of crustal

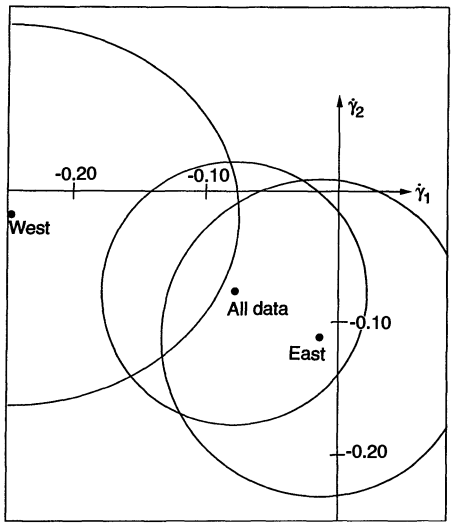

Fig. 2. Representation of results in strain rate ($\dot{\gamma}_1$, $\dot{\gamma}_2$) space. Estimated strain for the entire network; eastern and western subnets are shown. Circles represent a posteriori 95% confidence intervals. Strain rates are significant at the 95% level if the confidence interval excludes the origin.

shear strain results from lower crustal ductile slip (*4*, *25*). In theory, it is a straightforward matter to compare the measured rate of strain accumulation in the NMSZ with the rate at which strain is estimated to have been released over time in large historic and prehistoric earthquakes. Without instrumental recordings of the past large earthquakes, however, estimation of their moment (the slip area times the average displacement) is difficult. From the distances at which damage occurred and at which shaking was felt at the time of the 1811 to 1812 earthquakes, it has been estimated that slip was about 5 to 8 m (*26*) in those earthquakes. By the displacement inversion from angle changes (*23*), we estimated the slip rate to be about 5 to 7 mm per year; hence, it takes about 1000 years to accumulate the strain energy to have an earthquake similar to the 1811 to 1812 events. Paleoseismological studies indicate that the recurrence rate for large earthquakes in the New Madrid region may be on the order of 500 to 1000 years. Russ (*27*) estimated that the recurrence interval for large earthquakes from soil liquefaction was about 600 to 700 years. Saucier (*3*) dated two strong prehistoric earthquakes in Towosahgy, about 30 km northeast of New Madrid, and found that the first one occurred about 100 years before A.D. 539 and a probable second one sometime between A.D. 539 and 991 (*28*). It is not known if these prehistoric earthquakes are the result of repeated slip of the same fault; however, if this were the case, then 5 to 8 m of slip every 500 to 1000 years would require intraplate strain accumulation at a strain rate of about 0.1 microstrain per year, similar to the measured rate in the Caruthersville network.

Although it is somewhat surprising that a high strain rate was observed in such an intraplate region, this could simply be an indication that there are several major northeast-trending, right-lateral fault zones in this area. By analogy with areas along the San Andreas fault, subparallel strike slip faults could result from distributed ductile shear at depth (*29*). The western subnet lies across the fault zone coincident with the northwest boundary of the rift, which may have been responsible for the major earthquake that occurred near New Madrid. Evidence of a linear feature along which liquefaction occurred, termed the Bootheel lineament, has been found by Schweig and Marple (*30*) about halfway between the seismicity zone in the center of the rift and the northwest boundary of the rift. The seismic potential of these features deserves special attention in view of the results reported here.

We considered the possibility that the observed strain rates were due to postseismic lower crustal flow in response to the great 1811 to 1812 earthquakes, rather than strain accumulation associated with impending earthquakes. It appears, however, that the spatial distribution of strain is inconsistent with the 1811 to 1812 postseismic effects. The observed broad zone of strain implies a short lower crustal relaxation time, roughly one-tenth (or less) of the elapsed time since the last great earthquake (about 160 years to 1972, the time midway between the two surveys) (*31*), on the order of that observed in California (*32*). With such a short relaxation time, any postseismic deformation would have decayed long before triangulation surveys in the 1950s. In contrast, if the lower crustal relaxation time was quite long compared to the approximately 160-year elapsed time, the strain rate would be quite localized near the fault zone and would change sign with distance (*31*).

The rapid rate of deformation found in this region cannot be sustained for long periods of geologic time (hundreds of thousands to millions of years) because appreciable fault offsets would accumulate that are not observed in either geological or geophysical studies (*33*). Thus, from a geological perspective, the apparently rapid occurrence of large earthquakes in intraplate seismic zones is a transient phenomenon. Understanding this transience may be an important clue in understanding the mechanisms responsible for large intraplate earthquakes. If high rates of strain accumulation between large earthquakes are typical of other intraplate seismic zones, rapid strain accumulation may be a useful discriminant for identifying regions that may have large earthquakes in the future despite a historic absence of large earthquakes. In this regard, the high strain rate previously identified in the New York to Connecticut area (*4*) is especially noteworthy.

REFERENCES AND NOTES

1. As pointed out by J. Morgan [paper presented at the Symposium on Geodynamics, Texas A & M University, College Station, TX, 22 to 24 April 1987], average intraplate strain rates must be less than about 10^{-9} to 10^{-10} per year. If average intraplate strain rates exceeded this rate over long periods of geologic time, plate reconstructions would not be possible.
2. D. Amick and R. Gelinas, *Science* **251**, 655 (1991).
3. R. T. Saucier, *Geology* **19**, 296 (1991).
4. See discussion in M. D. Zoback, W. H. Prescott, S. W. Krueger, *Nature* **317**, 705 (1985).
5. A. C. Johnston and S. J. Nava, *J. Geophys. Res.* **90**, 6737 (1985).
6. A. C. Johnston and L. R. Kanter, *Sci. Am.* **262**, 68 (March 1990).
7. L. Himes, W. Stauder, R. B. Herrmann, *Seismol. Res. Lett.* **59**, 123 (1988).
8. M. D. Zoback *et al.* [*Science* **209**, 971 (1980)] discussed faulting revealed by seismic reflection profiling in the area of current seismicity. The boundaries of the rift zone shown in Fig. 1 were determined from modeling of aeromagnetic data.
9. T. G. Hildenbrand *et al.*, *U.S. Geol. Surv. Prof. Pap. 1236* (1982), p. 39. Abundant other geophysical and geological data confirm the existence of this rift, which is sometimes referred to as the Reelfoot Rift [see discussion by F. McKeown (*ibid.*, p. 1) and other papers in that publication].
10. O. W. Nuttli, *Bull. Seismol. Soc. Am.* **63**, 227 (1973).
11. R. B. Herrmann and J. Canas, *ibid.* **68**, 1095 (1978).
12. M. D. Zoback and M. L. Zoback, *Science* **213**, 96 (1981); M. L. Zoback and M. D. Zoback, in *Geophysical Framework of the Continental United States*, L. C. Pakiser and W. D. Mooney, Eds. (Geological Society of America, Boulder, CO, 1989), pp. 523–539; R. L. Dart and H. S. Swolfs, *Eos* **72**, 264 (1992).
13. The triangulation data were obtained from the NGS database.
14. F. C. Frank, *Bull. Seismol. Soc. Am.* **56**, 35 (1966).
15. J. L. Davis, W. H. Prescott, J. L. Svarc, K. J. Wendt, *J. Geophys. Res.* **94**, 13635 (1989).
16. M. Rothacher *et al.*, *Bernese GPS Software* (Version 3.2, Documentation April, Berne University, Berne, Switzerland, 1990).
17. A. Leick, *GPS Satellite Surveying* (Wiley-Interscience, New York, 1990).
18. H. M. Bibby, *Tectonophysics* **82**, 161 (1982).
19. A. R. Drew and R. A. Snay [*ibid.* **162**, 331 (1989)] discussed the simultaneous reduction method at length. We used this method to compute the two shear strain components defined in the text with the relation

$$\begin{bmatrix} \phi_n(t) \\ \lambda_n(t) \\ h_n(t) \end{bmatrix} = \begin{bmatrix} \phi_n(t_0) \\ \lambda_n(t_0) \\ h_n(t_0) \end{bmatrix} + \begin{bmatrix} C_{\phi\phi} & C_{\phi\lambda} \\ C_{\phi\lambda} & C_{\lambda\lambda} \\ C_{h\phi} & C_{h\lambda} \end{bmatrix} \begin{bmatrix} \phi_n(t_0) - \phi_0 \\ \lambda_n(t_0) - \lambda_0 \end{bmatrix} (t - t_0)$$

where $\phi_n(t)$, $\lambda_n(t)$, and $h_n(t)$ denote the geodetic latitude, geodetic longitude, and ellipsoidal height of the nth station at time t; t_0 denotes reference time, and ϕ_0 and λ_0 represent the reference position. The six crustal dynamic parameters, $C_{\phi\phi}$, $C_{\phi\lambda}$, $C_{\lambda\phi}$, $C_{\lambda\lambda}$, $C_{h\phi}$, and $C_{h\lambda}$ are directly related to the four strain rate components and two vertical tilt rates.
20. W. H. Prescott, *Bull. Seismol. Soc. Am.* **66**, 1847 (1976).

21. We estimated the precision of the GPS baseline vectors by adjusting the two surveys for common coordinates. The solution covariance matrices obtained from the GPS processing software were then scaled so that the weighted residual sum of squares divided by the number of degree of freedom was 1.0.
22. W. Thatcher, *U.S. Geol. Surv. Prof. Pap. 1515* (1991), p. 189.
23. Following the methods of P. Segall and M. V. Mathews [*J. Geophys. Res.* **93**, 14954 (1988)].
24. R. A. Snay, J. F. Ni, H. C. Neugebauer, in preparation.
25. J. C. Savage and R. O. Burford, *Bull. Seismol. Soc. Am.* **60**, 1877 (1970).
26. O. W. Nuttli, *ibid.* **73**, 519 (1983).
27. D. P. Russ, *U.S. Geol. Surv. Prof. Pap. 1236* (1982), p. 95.
28. In possible contradiction with the results presented in (*3*) (*27*), no evidence of paleoliquefaction effects was found in a series of drainage ditches in the southern NMSZ (S. G. Wesnousky and L. M. Leffler, in preparation). However, the absence of paleoliquefaction features does not demonstrate that prehistoric earthquakes did not occur.
29. Analysis of crustal deformation data just north of the San Francisco Bay by W. Prescott and S.-B. Yu [*J. Geophys. Res.* **91**, 7475 (1986)] indicates that right-lateral slip on the San Andreas fault and several subparallel right-lateral strike slip fault zones result from lower crustal ductile deformation distributed over a zone approximately 50 km wide.
30. E. S. Schweig III and R. T. Marple, *Geology* **19**, 1025 (1991).
31. W. M. Elsasser, in *The Application of Modern Physics to the Earth and Planetary Interiors*, S. K. Runcorn, Ed. (Wiley-Interscience, New York, 1969), pp. 223–244.
32. W. Thatcher, *J. Geophys. Res.* **88**, 5893 (1983).
33. For example, seismic reflection profiling in the New Madrid area has revealed remarkably little deformation of the unconformity between Paleozoic bedrock and Upper Cretaceous through Cenozoic Coastal Plain sediments (*8*); R. M. Hamilton and M. D. Zoback, *U.S. Geol. Surv. Prof. Pap. 1236* (1982)], p. 55.
34. In Table 1, the uncertainties are 1 SD, based on the a priori data errors. σ_0 refers to the a posteriori SD of an observation of a priori unit weight (*2, 3*) [also see, for example, R. Snay, *J. Geophys. Res.* **91**, 12695 (1986)]. We calculated a posteriori SDs by multiplying the SEs in Table 1 by σ_0. Confidence intervals of 95% for $\dot{\gamma}$ were estimated by Monte Carlo simulation. Gaussian random variables with means equal to observed values of $\dot{\gamma}_1$ and $\dot{\gamma}_2$ and variances equal to the a posteriori variances were drawn to simulate $\dot{\gamma}$ according to Eq. (*1*). An independent analysis of the data from the western subnetwork by R. Snay of the NGS yielded essentially the same strain rate as presented in Table 1.
35. We thank W. H. Prescott and M. Lisowski for help with this study, and R. A. Snay for cooperation. A. Johnston and J. Savage made useful comments on an earlier version of this manuscript. This work was supported by U.S. Geological Survey grant 14-08-0001-G1943-02.

17 March 1992; accepted 15 July 1992

Exsolution of Hornblende and the Solubility Limits of Calicum in Orthoamphibole

Eugene A. Smelik and David R. Veblen

Exsolution between orthorhombic and monoclinic amphibole has been postulated for many years on the basis of crystal-chemical and structural differences. Transmission and analytical electron microscope examination of calium-rich gedrite specimens from southwestern New Hampshire has now revealed evidence for exsolution of calcic clinoamphibole (hornblende) from ferromagnesian orthoamphibole. Analytical electron microscopy data suggests that calcium has a low solubility limit in the orthoamphibole structure. The hornblende lamellae range from only a few unit cells in thickness to about 80 nanometers. The formation of the calcic amphibole lamellae resulted from heterogeneous nucleation and growth along pre-existing (100) stacking faults. Thus, the deformation processes producing the stacking faults played a key role in preparing the sites for exsolution.

Exsolution, sometimes called phase separation, unmixing, or precipitation, is a common and important process that occurs in a wide range of natural and synthetic solid solutions. Precipitation hardening is a primary method of strengthening in many metal alloy systems, especially in aluminum and magnesium alloys (*1*). Exsolution is equally important in glass and glass-ceramic systems for purposes of strengthening and purification (*2*). Controlling exsolution reactions and thus the characteristics of the resulting microstructures in metal, glass, and glass-ceramic systems allows for the production of many materials possessing a wide range of desirable properties.

Exsolution occurs in a wide range of natural mineral systems, especially the oxides and silicates. Exsolution microstructures in minerals not only change the mineral's physical properties, but they also serve as a record of the postcrystallization mineral behavior. The characterization of exsolution microstructures in silicate mineral systems has provided a more complete understanding of the crystal chemistry and behavior of complex, multicomponent solid solutions. In addition, exsolution microstructures are potentially useful tools for unraveling pressure-temperature-time histories of igneous and metamorphic rocks. The increased use of transmission and analytical electron microscopy (TEM/AEM) in mineralogy in recent years has provided much new evidence for exsolution in many silicate systems, such as feldspars, pyroxenes, amphiboles, and micas (*3*). Moreover, TEM/AEM techniques allow for the detailed crystallographic and crystal-chemical characterization of fine-scale precipitates and in many instances provide clues for the exsolution mechanisms responsible for the microstructures. Results from such studies are especially useful in that reaction rates of many silicate exsolution reactions are too slow to study in the laboratory. In this report we provide evidence for exsolution between two members of the amphibole mineral group (double-chain silicates), specifically between ferromagnesian orthorhombic amphiboles in the anthophyllite-gedrite series and the monoclinic calcic amphibole, hornblende.

In the analogous pyroxene system (single-chain silicates), it is common for ferromagnesian orthopyroxenes to contain exsolution lamellae of the Ca-rich clinopyroxene augite along (100) (*4*). Because of the close chemical and structural similarities between pyroxenes and amphiboles, one would expect that similar exsolution phenomena should occur between calcic clinoamphiboles and orthoamphiboles. Despite the abundance of orthoamphibole-bearing rocks from high-grade metamorphic terranes and numerous studies of coexisting orthoamphiboles and clinoamphiboles, such exsolution microstructures have not been reported (*5*).

Using TEM and AEM (*6*), we examined *Pnma* orthoamphibole samples from the "Amphibole Hill" area of southwestern New Hampshire (*7*). The orthoamphiboles come from sillimanite-staurolite grade amphibolites consisting primarily of coexisting, coarse-grained hornblende and orthoamphibole (*8*). Visible light microscopy of the coarse hornblende crystals shows abundant exsolution lamellae of primitive, $P2_1/m$ cummingtonite along (100) and $(\bar{1}01)$ (*9*), whereas the orthoamphiboles appear to be homogeneous.

When examined with the electron microscope, the orthoamphiboles were found to be completely exsolved; they consist of coherently intergrown lamellae of anthophyllite and gedrite. The orthoamphibole exsolution lamellae have orientations that range from (010) to (120) (*10, 11*). Punctuating the anthophyllite-gedrite exsolution texture are lamellae of hornblende reaching maximum thicknesses of 60 to 80 nm (Fig. 1). The hornblende lamellae appear to be coherently intergrown exactly along (100) as shown by the [001] high-resolution TEM (HRTEM) image shown in

E. A. Smelik, Department of Geological and Geophysical Sciences, Guyot Hall, Princeton University, Princeton, NJ 08544.
D. R. Veblen, Department of Earth and Planetary Sciences, Johns Hopkins University, Baltimore, MD 21218.